Macromolecules
PERSPECTIVE

Macromolecules **2010**, *43*, 1675–1688 **1675**
DOI: 10.1021/ma902035p

Transmission Electron Microtomography and Polymer Nanostructures

Hiroshi Jinnai,*,†,‡ Richard J. Spontak,§ and Toshio Nishi‡

†*Department of Macromolecular Science and Engineering, Graduate School of Science and Engineering, Kyoto Institute of Technology, Kyoto 606-8585, Japan,* ‡*WPI Advanced Institute for Materials Research, Tohoku University, Sendai 980-8577, Japan, and* §*Department of Chemical & Biomolecular Engineering and Materials Science & Engineering, North Carolina State University, Raleigh, North Carolina 27695*

Received September 11, 2009; Revised Manuscript Received January 18, 2010

ABSTRACT: This Perspective summarizes the recent advances and perspective in three-dimensional (3D) imaging techniques and their applications to polymer nanostructures, e.g., microphase-separated structures of block copolymers. We place particular emphasis on the method of transmission electron microtomography (TEMT). As a result of some recent developments in TEMT, it is now possible to obtain *truly quantitative* 3D images of polymer nanostructures with subnanometer resolution. The introduction of scanning optics in TEMT has made it possible to obtain large volumes of 3D data from a micrometer thick polymer specimens using conventional electron microscopes at relatively low acceleration voltage, 200 kV. Thus, TEMT covers structures over a wide range of thicknesses from a few nanometers to several hundred nanometers, which corresponds to quite an important spatial range for hierarchical polymer nanostructures. TEMT provides clear 3D images and a wide range of new structural information, which cannot be obtained using other methods, e.g., conventional microscopy or scattering methods, can be *directly* evaluated from the 3D volume data. In addition, when combined with other characterization methods, e.g., scattering and computer simulations, TEMT can yield even better results. The single chain conformation of block copolymers inside microdomains may be virtually visualized by TEMT. TEMT is a versatile technique that is not only restricted to polymer applications but can also be used as a powerful characterization tool in energy applications, e.g., fuel cells, etc.

1. Introduction

Polymer materials are ubiquitous in our daily life. They often consist of more than one species of polymers and, therefore, can be called multicomponent systems, e.g., polymer blends[1−4] and block copolymers.[5,6] Because of the repulsive interaction between the constituent polymers, multicomponent polymer materials often show "phase separation". Organic−inorganic composites are another class of polymer-based multicomponent materials that have attracted considerable interest of researchers because they often exhibit unexpected properties synergistically derived from the constituents.[7,8] Nanometer-sized particulate fillers, e.g., carbon black (CB), silica (Si) nanoparticles, etc., are known to form hybrids with organic polymers, which show a significant increase in their static and dynamic moduli,[9] strength,[10] and thermal and electrical conductivities.[11,12]

The number of studies carried out to characterize such multicomponent nanometer-scale polymer structures (hereafter called "nanostructures") has been significantly increasing over the past couple of decades. Academic interest in complex fluids (to which polymeric systems belong) as well as the continuous industrial demand for new materials have triggered such studies. Pattern formation and self-assembling processes of polymer blends have been widely researched for studying nonlinear nonequilibrium phenomena. Block copolymers self-organize to form (equilibrium) highly periodic nanometer-scale domains ("microphase-separated domains" or simply "microdomains"). A deep understanding of the "structure−property relationship" in multicomponent polymer nanostructures is of significant importance for industrial applications of these nanostructures: carrying out basic studies on this relationship will aid in designing new polymer materials with superior physical properties that satisfy the diverse requirements of industries.

Thus, morphological studies of the multicomponent polymeric materials have been carried out by employing microscopy and scattering methods. Commercially available optical microscopes, transmission electron microscopes (TEMs), scanning electron microscopes (SEMs), and atomic force microscopes (AFMs) have been widely used in these studies. The biggest advantage of microscopy is that it provides intuitive real-space representations of morphologies. However, when it comes to "measurements", especially in the case of quantitative measurements, microscopy may lack statistical accuracy due to the small field of view. In contrast, scattering methods usually provide considerably superior statistical accuracy simply because the larger observation volume. It should be, however, noted that scattering methods often require "(hypothesized) models" beforehand for data analyses. They *do not* provide any intuitive insights into morphologies, as microscopy does. After all, for the complete characterization of a specific morphology, the morphology has to be first obtained by microscopy and subsequently by scattering for the evaluation of structural parameters on the basis of the morphology. Thus, microscopy and scattering are complementary.

With the advances in precision polymerization,[13−16] polymer nanostructures, especially microphase-separated structures, are becoming increasingly complex. The identification of such complex morphologies is difficult because conventional microscopes provide only two-dimensional (2D) (transmitted or surface) images of three-dimensional (3D) objects. These 2D images are not useful as the nanostructures are becoming complex, which

*To whom correspondence should be addressed: e-mail hjinnai@kit.ac.jp.

Published on Web 01/28/2010

consequently makes the interpretation of the accompanying scattering data difficult. Therefore, new microscopes that are capable of obtaining 3D images of nanostructures have to be developed. We hereafter call the technique involving the use of such microscopes as "3D microscopy".

In the present study, we focus on the 3D microscopy technique, transmission electron microtomography (TEMT). This Perspective is organized in the following manner. In section 2, various 3D microscopy techniques including TEMT are introduced, and their features and spatial resolutions are briefly described.

Hiroshi Jinnai was born in 1965 in Osaka, Japan. He received his B.S. (1988), M.S. (1990), and Ph.D. (1993) degrees in polymer physics from Kyoto University under the direction of Professor Takeji Hashimoto. During this period, he was a guest scientist twice at National Institute of Standards and Technology (NIST), USA, from 1988 to 1989 and from 1991 to 1992 under the guidance of Dr. Charles C. Han. He received a JSPS (Japan Society for the Promotion of Science) Research Fellowships for Young Scientists in 1993. In 1993, he joined an ERATO (Exploratory Research for Advanced Technology) program, Hashimoto Polymer Phasing Project, as a group leader. He was appointed Lecturer at the Department of Macromolecular Science and Engineering of Kyoto Institute of Technology in 1998 and was promoted to Associate Professor in 2002. He is Adjunct Professor of World Premier Institute (WPI)-Advanced Institute for Materials Research (AIMR) from 2009. He was awarded the SPSJ (The Society of Polymer Science, Japan) Wiley Award in 2006. He is the first Japanese ever to win the biannual Ernst-Ruska-Prize in 2007. This international award, named after Ernst Ruska, winner of the 1986 Nobel Prize for his invention of the transmission electron microscope, is given by the Deutschen Gesellschaft für Elektronenmikroskopie e.V. (German Society of Electron Microscopy). He is also the recipient of the 2008 Award for Persons of Merit in Industry-Academia-Government Collaboration in FY2008 (Minister of Education, Culture, Sports, Science and Technology Award). His research interests are the self-assembling morphologies and processes of polymer blends and block copolymers.

Dr. Richard J. Spontak is an Alumni Distinguished Professor of Chemical & Biomolecular Engineering and Materials Science & Engineering at North Carolina State University. A fellow of the American Physical Society, Spontak received the B.S. degree in Chemical Engineering (with honors/high distinction) from the Pennsylvania State University in 1983 and was later awarded the Ph.D. degree in Chemical Engineering from the University of California at Berkeley in 1988. He pursued postdoctoral research in Materials Science & Metallurgy at the University of Cambridge and then in Condensed Matter Physics at the Institutt for Energiteknikk (Norway) before joining the Corporate Research Division of the Procter & Gamble Company in 1990. He accepted a faculty position at North Carolina State University in 1992. Since that time, he has published over 250 research papers, and his work has been featured on the cover of 15 journals and 1 book. His research interests relate to the phase behavior and morphology/property development of nanostructured polymers, polymer blends and nanocomposites, and organogels as well as novel uses of electron microscopy (including electron microtomography) in polymer science. In recognition of his recent research endeavors, he is the recipient of Alexander von Humboldt and Tewkesbury fellowships, the 2006 American Chemical Society (PMSE Division) Cooperative Research Award (with S.D. Smith), the 2007 German Society for Electron Microscopy Ernst Ruska Prize (with H. Jinnai and P.A. Midgley), and the 2008 American Chemical Society (Rubber Division) Chemistry of Thermoplastic Elastomers Award. He is or has been on the editorial advisory board of nine international journals, including *Macromolecules* and *Langmuir*. Spontak is also an acclaimed educator and academic mentor. For his efforts promoting cooperative/active classroom learning and multidisciplinary undergraduate research/design, he has received the 2008 Board of Governor's Award for Excellence in Teaching, the highest educational honor bestowed by the University of North Carolina system, as well as the 2006 International Network for Engineering Education & Research Recognition Award and the 2009 American Society for Engineering Education (Southeast Region) Outstanding Mid-Career Teaching Award.

Toshio Nishi was born in Kanagawa, Japan, in 1942, and graduated from the Department of Applied Physics of The University of Tokyo (UT), Japan, in 1965. He studied polymer physics and awarded Master of Engineering in 1967 and Doctor of Engineering in 1972 at the same university. He joined R&D Division of Bridgestone Tire Co., Ltd., in 1967 until 1980. He was a visiting scientist at Bell Telephone Laboratories, USA, from 1972 to 1975. He was appointed Lecturer at the Department of Applied Physics, UT, in 1980 and Associate Professor in 1982 and promoted to Professor in 1992, majoring in physics of polymer alloys and composites. In 2003, he retired from UT and was appointed as Emeritus Professor of UT. He then moved to Tokyo Institute of Technology (TIT) and had studied polymer nanotechnology. In 2008, he again retired from TIT and appointed as Emeritus Professor of TIT. Then, he was asked to move to newly created WPI-AIMR, Tohoku University, as Full Professor and Principal Investigator. He served as President of The Society of Rubber Industry, Japan, from 1995 to 1997 and as Vice President of The Society of Polymer Science, Japan, from 2000 to 2002. He was awarded the Polymer Science Award in 1990, Oenschlager Award in 1998, Polymer Science Merit Award in 2005, and received International Rubber Conference Organization Medal in 2009. He is active in the field of polymer nanotechnology and polymer megatechnology like seismic−elastomeric isolators. He is also active as a Specialist to The Supreme Court in the field of polymer science and engineering.

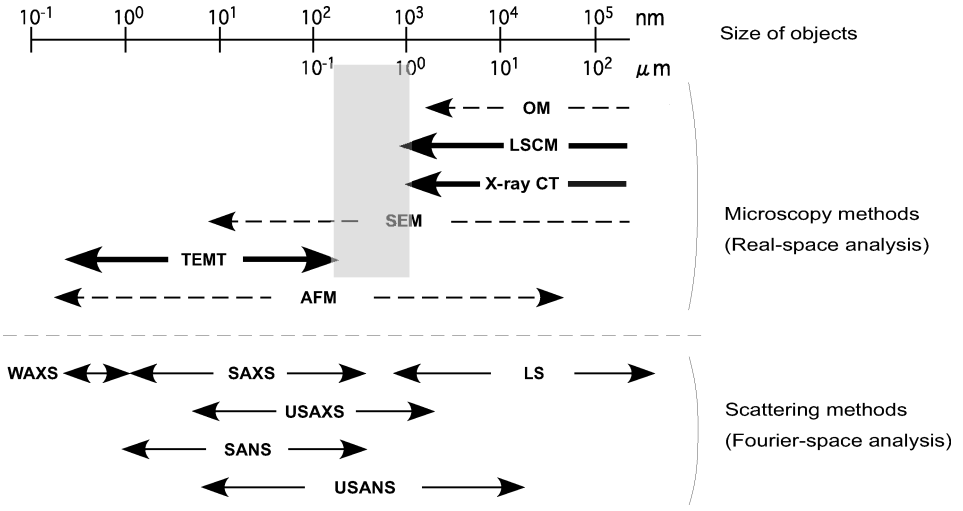

Figure 1. Schematic illustration showing resolution of both microscopy and scattering methods. Abbreviations are as follows: OM (optical microscopy), LSCM (laser scanning confocal microscopy), X-ray CT (X-ray computerized tomography), SEM (scanning electron microscope), TEMT (transmission electron microtomography), AFM (atomic force microscopy), WAXS (wide-angle X-ray scattering), SAXS (small-angle X-ray scattering), LS (light scattering), USAXS (ultrasmall-angle X-ray scattering), SANS (small-angle neutron scattering), and USANS (ultrasmall-angle neutron scattering). Methods shown by the bold arrows are 3D microscopy techniques. The shaded region represents the "missing spatial region" in 3D microscopy.

In section 3, recent developments in TEMT with respect to quantitative measurements are mentioned. New TEMT with scanning optics developed using a conventional TEM with an acceleration voltage of 200 kV for imaging thick polymer specimens of the order of micrometer is also explained. It is important to use both real-space methods (i.e., microscopy) and Fourier-space methods (i.e., scattering) together to characterize complex polymer morphologies. In this study, we propose the combination of these two complementary methods for polymer nanostructure characterization. In section 4, some representative examples of TEMT for polymer nanostructures are presented. An example of use of TEMT for energy applications is included in this section. Possible future studies and research areas using TEMT are also discussed.

2. 3D Microscopy

Figure 1 shows the spatial resolution of various types of microscopy and scattering methods, including 3D microscopy techniques such as laser scanning confocal microscopy (LSCM), X-ray computerized tomography (X-ray CT), and TEMT. LSCM has been extensively used to investigate the phase-separated "bicontinuous" structures of polymer blends.[3] It should be noted that X-ray CT is particularly useful for *opaque* specimens with micrometer-sized structures, while transparent specimens are necessary for LSCM. X-ray CT has been also extensively used in medical science.[17,18] In the early 1990s, the spatial resolution of X-ray CT was limited to ca. 100 μm. Recently, the resolution has substantially improved and is now comparable with ($\sim$1 μm) or even superior to that of optical microscopy. Figure 2 shows an example of morphological investigation of a fiber reinforced plastics (FRP) under uniaxial extension using X-ray CT with a homemade uniaxial tensile testing instrument. Three 3D images at the same volume of the FRP specimen were taken as a function of strain, in which the formation of the voids around the fibers were clearly observed.[19] We here note that the stress values from the FRP are simultaneously obtained as the specimen is stretched and the corresponding 3D image is taken. Such combination of the mechanical properties together with the internal morphologies of the materials is of great significance in understanding the structure−property relationship.

One of the biggest drawbacks of employing X-ray CT for polymers is, however, that the X-ray absorption coefficient is small and very weakly depends on the type of species. Thus, (chemical) treatment, e.g., labeling or etching, is often required for contrast enhancement. The X-ray phase shift induced by polymers, on the other hand, is significantly large. X-ray phase tomography measures such X-ray phase shift and reconstructs a tomogram that maps the refractive index difference, which is roughly proportional to the mass density of polymers.[20] Thus, X-ray phase tomography is potentially superior to the conventional (absorption) X-ray CT. NMR, which has a resolution of ca. 20 μm (not shown in Figure 1), is used for 3D imaging.[21]

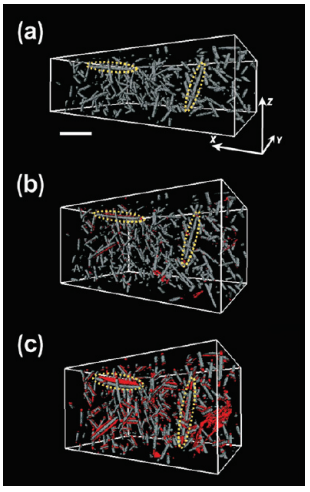

Figure 2. 3D images of a fiber reinforced plastics (FRP) under uniaxial extension (extension rate: 0.1 mm/min). The images were taken using X-ray CT equipped with a homemade uniaxial tensile testing machine. The strains are (a) 0 (quiescent state), (b) 20%, and (c) 60%. The gray rods are glass fibers. The red and transparent regions are voids and matrix polymer, respectively. Two representative fibers, parallel and perpendicular to the uniaxial direction, z, at each strain are indicated by dashed ellipsoids. The scale bar is 200 μm. Data obtained by using ELE SCAN (NITTETSU ELEX Co., Ltd., Japan).

Because most of the polymer materials have hierarchical structures, not only nanoscale structures but also their higher-order structures in the submicrometer scale ("mesoscale") are important. The shaded region in Figure 1, corresponding to the

mesoscale, is the missing spatial region in 3D microscopy. This spatial gap spans from a few tens of micrometers to a couple of micrometers, which is "too large" for TEMT and "too small" for X-ray CT and LSCM. With the recent development in X-ray optics, the highest resolution of X-ray CT has approached several dozens of nanometers. Coherent X-ray diffraction microscopy,[22] which is a lensless phase-contrast imaging technique, may also be another candidate for the mesoscale 3D observations. The setup of this new imaging method is close to that of the small-angle X-ray scattering. The coherently diffracted wave is related to the sample electron-density map by Fourier transform, and the phase of the diffracted wave, which is not directly measurable in the scattering experiments, is retrieved using an iterative method.[23,24] The coherent X-ray diffraction microscopy was actually used to observe an unstained human chromosome.[22]

In TEMT, 3D imaging of thick polymeric specimens of the order of a micrometer is now becoming practical using lab-based 200 kV TEM.[25,26] The latter will be briefly described in section 3. B. Although these attempts to fill the spatial gap are yet in the preliminary stage, the 3D structural characterization of polymeric materials over a wide range from nanometers to millimeters will be realized in the near future. We note that there are some "destractive" 3D imaging methods, in which stripping of the surface of the specimen and the subsequent imaging of the exposed surface are iterated so that a series of 2D images at different depth can be obtained.[27−30] Low-pressure plasma treatment,[28] focused ion beam (FIB) treatment,[27,29] and ultramicrotoming[30] are used for stripping the surface of specimens, while scanning force microscopy and scanning electron microscopy are used for surface imaging.

3. Recent Developments in TEMT and Its Perspective

In this section, recent developments in TEMT are discussed. As mentioned before, TEMT is based on tomography. Let us first start with the history of tomography. The need to obtain a higher-dimensional "structures" using lower-dimensionality data is present in many fields of physical and life science. This concept was first applied in the field of astronomy.[31] A method was proposed for the reconstruction of a 2D map of solar microwave emissions from a series of 1D radio telescope data. In 1963, a study on the potential of tomography for application in medicine stimulated interest in tomographic reconstruction.[32] The development of the X-ray computed tomography scanner was based on Cormack's work,[33] for which Cormack and Hounsfield received a joint Nobel Prize in 1979. The first tomographic reconstruction from electron micrographs can be traced to 1968,[34−36] which was followed by the publication of a number of theoretical papers discussing the theoretical limits of Fourier techniques,[37] approaches to real-space reconstruction,[38,39] and iterative reconstruction routines.[40−42] Although the theory rapidly advanced, developments in experiments were slow. The limiting factors are beam damage, the poor performance of goniometers, and large computing power required for image processing and reconstruction. Among these factors, the last two have been addressed, but the beam damage is still a serious problem.

In the case of TEMT, projections at different angles are recorded by tilting the specimen with respect to the electron beam in the TEM column. The projections are carefully aligned about the tilt (rotation) axis and then reconstructed to generate 3D images.[43−47] The achievable tilt range in a TEM is restricted by the small space between the specimen holder and the objective lens; they will come in contact with each other at a large tilt angle, e.g., 70°. The missing information due to this angular limitation is indicated by a wedge-shaped region in the Fourier space, i.e., *the missing wedge*, giving rise to a loss of resolution of the reconstructed image, especially in the direction parallel to the electron beam. This intrinsic but serious problem of TEMT has remained unsolved for the past two decades. An experiment to solve (or reduce) the missing wedge problem is presented in section 3.A. For further details about TEMT, an excellent book entitled "Electron Tomography"[43] and few review papers[44−47] are available.

A. Truly Quantitative TEMT. As mentioned previously, the limitation of the angular range in experiments results in the missing wedge of structural information in the Fourier space. Because of this limitation, the resolution along the direction parallel to the optical axis of the microscope (the plane perpendicular to the plane of the specimen), i.e., the Z-direction, is lower as compared to that in the specimen plane.[44,48,49] In addition, a critical effect of the missing wedge is that the 3D reconstruction of elongated objects in the specimen plane strongly depends on their angle relative to the tilt axis. For example, cylindrical microdomains in the block copolymer morphology that are perpendicular to the tilt axis of the specimen may not be imaged by 3D reconstruction.[50]

One of the most effective solutions of this problem is to minimize the volume of the missing wedge by employing another tilt axis in addition to the first one ("dual-axis tomography"). Penczek et al.[51] pioneered dual-axis tomography for biological sections, followed by Mastronarde.[52] The unsampled volume in conventional single-axis tomography, i.e., the missing wedge, becomes the "missing pyramid" in dual-axis tomography (see Figure 2 in ref 50), which is *considerably* smaller than the missing wedge. The detailed protocol of dual-axis tomography and its *substantial* effects on the 3D visualization of the cylindrical microdomains can be found elsewhere.[50]

Although effective, dual-axis tomography requires tedious experimental protocols such as (i) two tilting experiments at the same volume of the sample and (ii) the combination of two 3D reconstructed data sets with high precision. Despite involving such protocols, the missing region in the Fourier space only reduces and does not vanish. In CT, it is advisable to tilt the specimen up to 90°. Such complete rotation has been first carried out using a high-voltage electron microscope (HVEM). In this study, a thin glass capillary is mounted concentrically on a regular single-axis tilt holder of an HVEM.[53] A biological specimen whose size is of the order of a few micrometers is mounted on the tip of the holder.

Realistically, scientists have limited access to the HVEMs, and moreover, it is a lot more beneficial for polymer research if such "missing-wedge-free TEMT" is combined with the conventional 200−300 kV TEM. Under such constraints, more sophisticated samples, e.g., needle-shaped specimens with diameters of ca. 100−200 nm, have to be prepared. This type of nanofabrication of materials has been quite difficult, especially in the case of "soft" polymer materials. In 2005, Niihara et al. reported the successful fabrication of a soft polymer material, a block copolymer, using the FIB method.[54] On the basis of the Niihara's results, Kawase et al. prepared a needle-shaped specimen of a zirconia/polymer nanocomposite with the diameter of 150 nm, which was attached to the tip of a specially modified specimen holder without any supporting film. They obtained complete set of tomograms generated from 181 projections that were measured over the angular range of ±90°.[49]

Figure 3a shows an electron micrograph of the needle-shaped specimen. The 5−20 nm sized zirconia grains appear as black domains in the polymer matrix. No obvious sign of damage occurred during the FIB fabrication process, such as melting of polymer matrix due to the intense gallium ion beam or the redeposition of contaminates, is observed on the surface of the needle-shaped specimen.

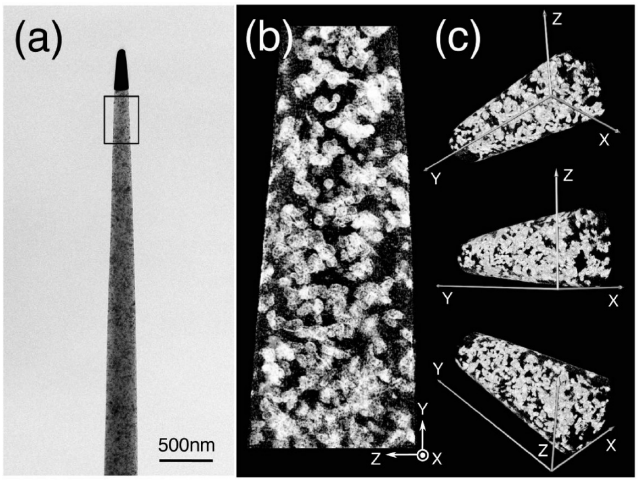

Figure 3. (a) Electron micrograph of needle-shaped polymer nanocomposite containing zirconia fillers. The rectangle indicates the position subjected to the TEMT experiment. (b) Volume-rendered and (c) surface-rendered 3D images of needle-shaped specimen from various viewing angles. The needle-shaped specimen whose diameter is 150 nm was made using an FIB system (FB2100, Hitachi, Ltd., Japan) at an acceleration voltage of 40 kV and mounted on a modified Mo grid for ±90° rotation. TEMT experiment was carried out using a JEM-2200FS (JEOL Ltd., Japan). In total, 181 electron micrographs from −90° to +90° in 1° increments were taken. The tilt series of the electron micrographs was precisely aligned by the fiducial marker method using the zirconia grains as markers, and then tomograms were made by the filtered back projection (FBP) method.[55] All the softwares for the alignment and reconstruction are homemade. Detailed experimental protocol can be found elsewhere.[49]

The 3D structure of the zirconia/polymer composite is shown in Figure 3 as a volume-rendered image (Figure 3b) and surface-rendered images from various viewing angles (Figure 3c). The white regions are corresponding to zirconia grains. Even though the zirconia domains appear to be continuous under TEM (see Figure 3a), it is clear from the TEMT 3D reconstruction that they form mostly separate domains and not intersecting domains.

Image artifacts prominently appear in the $X-Z$ plane (a plane perpendicular to the tilting axis of the TEM) due to the limitation of the angular range. Because we have the complete data set with ±90° angular tilting, it is worthwhile to show how the maximum tilt angle affects the image quality and resolution in TEMT experiments. A series of 3D reconstructions with various maximum tilt angles α are made. That is, 3D images are reconstructed from exactly the same TEM tilt series and alignment within the angular range of ±α. Figure 4a shows the $X-Z$ cross sections of the same region of the needle-shaped specimen from α = 40° to α = 90° with 5° increments. As α decreases, the image quality, especially the contrast between the zirconia grains and the polymer matrix, becomes worse, and the edge of the needle-shaped specimen becomes pear-shaped. Note that the angular range is normally limited to α = 60°−70° in conventional TEMT observations using planar sections.

Accurate determination of structural parameters, e.g., volume fraction ϕ, of zirconia grains is of particular interest. ϕ is measured as a function of α and is shown in Figure 4b. ϕ decreases as α increases and approaches a certain asymptotic value for a high α (α > 80°). The known composition of the zirconia grains is 0.055 ± 0.005 from the preparation of the sample (dotted line), which is in an excellent agreement with the measured asymptotic value. The elongation of the zirconia grains and the low signal-to-noise (S/N) ratio of the

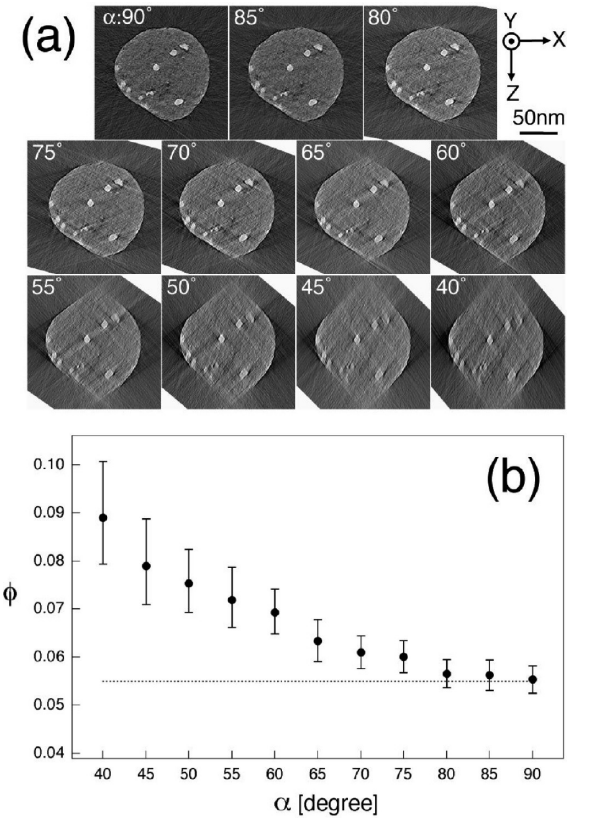

Figure 4. (a) Series of images of $X-Z$ cross sections of region of needle-shaped specimen reconstructed at various maximum tilt angles, α, from 40° to 90° with 5° increments. (b) Plot of volume fractions (zirconia/nanocomposite), ϕ, experimentally determined from 3D reconstruction series from α = 40° to α = 90°. The dashed line represents the known composition of zirconia grains. The error bars are associated with the uncertainty in the threshold of binarization.

tomograms may be the cause of the small deviation from the true value at small α values, which makes the binarization (in order to find the interface between the zirconia and polymer) of the tomogram somewhat difficult. It is worthwhile to note that we have observed 27% error in ϕ of our zirconia/polymer nanocomposite for conventional TEMT, i.e., α = 60°. Furthermore, we have found that the angular range of α ~ 70° (or α ~ 50° in dual-axis tomography) may be required in order to attain 10% error in ϕ of the nanocomposite.

B. Scanning Transmission Electron Microtomography: 3D Imaging in "Mesoscale". Let us describe another recent development in TEMT—new TEMT employed to cover mesoscale structures. As mentioned in section 2, there is a spatial gap in 3D microscopy (see Figure 1). In polymer science, the hierarchical nature of polymer structures has to be seamlessly examined from a few to several hundreds of nanometers. In block copolymer nanostructures, for example, the smallest structural elements, e.g., spheres, cylinders, lamellae, are of the order of several nanometers to several tens of nanometers, which can be examined by existing TEMT.[56−61] The upper-hierarchical structure of such structural elements is the grain. The size and internal domain orientation of the grains, the mesoscale structures, are too large to be observed by existing TEMT.

This is also true in the case of industrial samples. The nanocomposites consisting of nanoscale (particulate) fillers, e.g., carbon black and silica nanoparticles, and polymer matrix, primary particles form "aggregates" whose size spans from 100 nm to 1 μm. These aggregates further

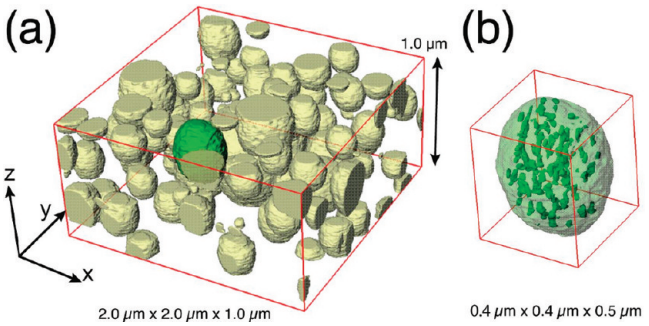

Figure 5. (a) 3D surface-rendered image of ultrathick specimen of ABS resin. The thickness of the specimen is ca. 1 μm. The optical axis of the electrons is along the Z-axis. The size of the box is 1980 nm × 1980 nm × 998 nm. One of the salami structures indicated by green color is magnified and shown in (b). This STEMT experiments was carried out on a JEM-2100 microscope (JEOL Ltd., Japan) with a LaB_6 electron gun. The accelerating voltage was 200 kV. The pixel resolution was 4.4 nm. A series of STEM micrographs with 512 × 512 pixel elements were acquired at tilt angles ranging form −60° to +60° in 2° increments. The electron optics of the JEM-2100 was tuned so that the effective focal depth in the STEMT experiments was 1600 nm. The experimental protocol, tilting of the ABS specimen, and subsequent imaging either by STEM were carried out using JEOL-developed software "TEMography". Detailed experimental protocol can be found elsewhere.[26]

assemble and form network structures called "agglomerates". Both aggregates and agglomerates contribute to the (mechanical) property of the nanocomposites; however, only aggregates can be studied by TEMT.[62] In order to fully understand the mechanical property of nanocomposite materials, 3D investigation of mesoscale "agglomerates" have to be carried out in 3D.

Thus, an extraordinary "ultrathick" specimen of the order of a few micrometers must be imaged in 3D either by TEMT or by X-ray CT for the mesoscale structural analysis. Quite recently, Aoyama et al.[63] and Loos et al.[25] independently reported 3D observations of thck biological and nanocomposite specimens by scanning TEM by using a 300 kV field emission gun as an electron source. They used microtomography along with scanning transmission electron microscopy (STEM). Let us call the technique scanning transmission electron microtomography (STEMT), in contrast to TEMT which we discussed so far. The main feature of STEMT is the optimization of the conversing angle of the electron beam for large focal length of electron optics. We note here that similar optics can be also realized in TEMT by changing the detection angle. The smaller the conversing (or detection) angle, the longer is the focal length of electron optics.

Figure 5 shows a 3D surface-rendered image of an ultrathick specimen of an acrylonitrile butadiene styrene (ABS) resin.[26] The ABS resin (TECNO ABS 330) was purchased from Technopolymer Co. Ltd., Japan. The thickness of the microtomed section is ca. 1 μm. The spatial distribution of OsO_4-stained polybutadiene (PB) spherical domains (often called "salami structures"), ranging from ca. 100 to 500 nm in diameter, can be clearly observed. Figure 5b shows a magnified image of a salami structure, which shows that the internal polystyrene/polyacrylonitrile domains are mostly discrete and not continuous.

In the above-mentioned experiment,[26] STEMT (at 200 kV acceleration voltage) is carried out with the acceptance angle for the detecter set to 6 mrad (bright field mode, BF-STEMT), indicating that transmitted and low-angle scattered electrons are used for the imaging. As compared to our study, the accepting angles in previous studies[25,63]

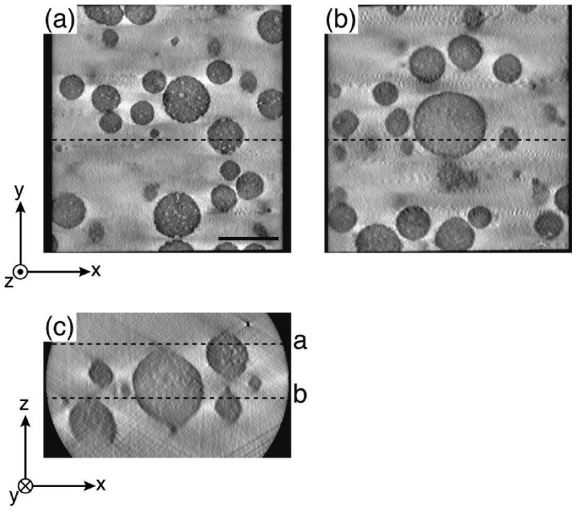

Figure 6. Cross-sectional images of the specimen shown in Figure 5a. The black parts indicate OsO_4-stained butadiene domains. The electron beam is along the Z-axis. (a, b) Cross-sectional "digitally sliced" images at different depths of 1 μm thick sample. The depths of $X-Y$ slices are indicated by dashed lines in (c). The electron beam was incident from the top, and hence, image (b) is obtained deeper inside the thick specimen. The detailed structures of the "salami" structure near the surface, i.e., part (a), appear to be clearer than those inside the specimen, i.e., part (b).[26]

were larger (dark-field mode, DF-STEMT). Contrast generation in STEM, especially in DF-STEM,[64] is rather complex; it is still uncertain which one of the two, i.e., BF- or DF-STEM, is better for polymer materials. In the case of ABS resin, BF-STEMT gives clearer image than DF-STEMT. In contrast to STEMT, the maximum observable thickness of ABS resin by TEMT (transmission mode) at low detection angle, 2.8 mrad, is found to be ca. 600 nm due to the severe blurring associated with the chromatic aberration of the optics.

A problem associated with STEMT is the beam broadening[65] in the sample. As the collimated electron beam goes through a thick specimen, electrons suffer multiple scattering thereby making the electron beam broader than when it enters the specimen. Thus, the resolution at deeper parts of the specimen becomes worse as compared to the surface (surface closer to the electron source); as a result, the cross-sectional images become blurred toward the bottom of the specimen, as shown in Figure 6.[26] One of the solutions of the beam broadening problem is to completely rotate, angular tilting = ±90° (as described in the previous section), the needle-shaped specimen of ABS resin with a few μm in diameter.[66]

The development of STEMT is still in the premature stage. STEMT has to be significantly developed for the practical application to polymers. It is interesting to point out that such development of 3D observation for ultrathick specimens is opposite direction of what the traditional electron microscopy has developed. In other words, STEMT pursues the large observation volume at the sacrifice of the resolution, while the traditional trend in the electron microscope has always pointed to higher resolution to achieve atomic resolution. Nevertheless, (S)TEMT for the mesoscale fills the "spatial gap" (the gray region in Figure 1) and carries out 3D imaging completely from submicrometers to millimeters.

C. Combination with Scattering Method. As mentioned in section 1, although the Fourier-space methods, i.e., scattering methods, are very powerful tool for statistically obtaining various structural parameters of polymer morphologies, they often require a hypothesized structural model for data analysis. Featureless scattering profiles, such as the profiles

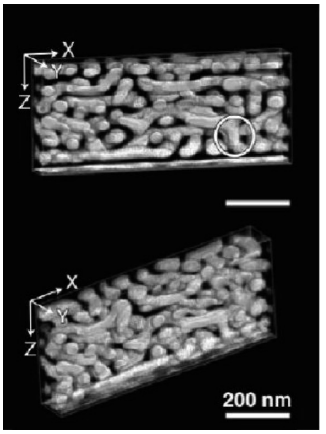

Figure 7. Volume-rendered 3D images of dPS-*b*-P2VP thin film from two different view points, in which dPS microdomain was made transparent. The box size of each 3D image is 720 nm × 90 nm × 344 nm. A series of TEM projections were acquired at tilt angles ranging from −50° to +50° in 1° increments. The tilt series were then aligned by fiducial marker method[68] using the Au particles and then reconstructed on the basis of the FBP method.[55] Detailed experimental protocol can be found elsewhere.[67]

without scattering peaks, are especially difficult to interpret. Even when a scattering peak exists, the characteristic length associated with the peak position is sometimes unknown. The real-space methods, especially 3D microscopy, are thus necessary to confirm the basic morphology of samples.

In this section, a block copolymer thin film with cylindrical morphology was investigated by a novel combination of neutron reflectivity (NR) and TEMT.[67] The block copolymer was poly(deuterated styrene-*block*-2-vinylpyridine) (dPS-*b*-P2VP). Figure 7 shows reconstructed 3D images of a dPS-*b*-P2VP thin film from two different view points, in which only the P2VP microdomain is shown (the dPS microdomain is transparent). Although the majority of the cylindrical microdomains were oriented parallel to the substrate and formed six layers, they did not form hexagonally packed cylindrical morphology (shown later in Figure 8a). Some of the cylindrical microdomains were aligned normal to the film surface and connected the adjacent layers (indicated by the white circle in Figure 7). The cylindrical microdomains appear to be interconnected through vertical cylinders.

The measured NR profile from the dPS-*b*-P2VP thin film, R_{exp}, is shown by the open circles in Figure 8, where the reflectivity R is plotted versus the magnitude of the scattering vector along the Z-direction, q_z [$q_z \equiv (4\pi\lambda) \sin\theta$]. Here, θ is the scattering angle. A *featureless* NR profile is obtained from the thin film, indicating that the microphase-separated structure inside the thin film is not highly ordered (as clearly shown in Figure 7).

As the first step to the analysis of R_{exp}, let us assume that the microphase-separated structure forms hexagonally packed cylindrical (HEX) microdomains in the thin film, as illustrated in Figure 8a. Although we already know that the microphase-separated structure in the thin film is not highly ordered (see Figure 7), the HEX model is the first choice because it is the easiest and simplest model for cylinder-forming block copolymers. The cylinders are assumed to be aligned parallel to the substrate according to the results from previous studies.[71,72] The hypothetical model is based on the structural parameters determined in the bulk state.[67] The scattering length density profile along the direction perpendicular to the film surface, i.e., along the Z-axis, is calculated from the model, b/v_{model}, which is then used to calculate the NR profile,

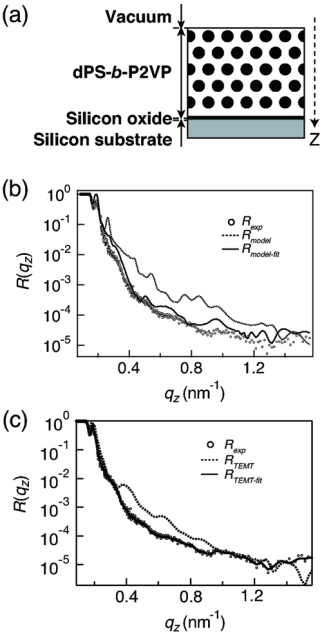

Figure 8. (a) Cross-sectional view of hypothesized initial model of dPS-*b*-P2VP thin film cast on Si substrate. The dark circles and white domain indicate the P2VP cylinders and dPS matrix, respectively (edge-on view). The Z-axis is normal to the film surface. (b) NR profile of dPS-*b*-P2VP thin film (open circles). The dashed line indicates the calculated reflectivity profile based on the hypothetical model (a). The dashed line is used as an "initial guess" in the fitting protocol.[69,70] (c) Reflectivity profile of dPS-*b*-P2VP thin film. The open circles indicate the measured NR profile. The dashed line and solid line represent the calculated reflectivity profile from the initial model obtained by TEMT and the best-fit reflectivity profile, respectively.

R_{model} (the dashed line in Figure 8). It is obvious that R_{model} does not reproduce the NR profile over the entire range of q_z. Subsequently, an algorithm based on a recursive calculation method[69,70] is employed to fit R_{model} to R_{exp}. Although the NR profile approaches R_{exp}, there is still a considerable deviation, especially for large q_z. This result again indicates that the microphase-separated morphology is not a simple one as hypothesized. Because the NR profile does not show distinctive peaks, it is intrinsically difficult to have a precise and unique best-fit profile unless we have a realistic model for the scattering length density b/v as the initial guess.

The scattering density profile along the Z-axis, b/v_{TEMT}, can be estimated from the 3D image in Figure 7. The detailed protocol of the estimation of b/v_{TEMT} from the 3D image can be found elsewhere.[67] The NR profile based on b/v_{TEMT} obtained from the TEMT experiments, R_{TEMT}, is shown in Figure 8c. From comparison with the previous results in Figure 8b, i.*e.*, R_{model}, it is found that R_{TEMT} exhibits a more accurate NR profile than R_{model}, indicating that b/v_{TEMT} (and thus TEMT) captures the global feature of the dPS-*b*-P2VP thin film morphology. b/v_{TEMT} is similarly used as the initial guess for the fitting. The resulting $R_{TEMT\text{-}fit}$ is denoted by solid lines in Figure 8c. $R_{TEMT\text{-}fit}$ shows an excellent agreement with R_{exp}, considerably better than R_{model}. We note here that the TEM 2D cross-sectional micrograph of the dPS-*b*-P2VP thin film does *not* provide a good initial guess model as the TEMT 3D volume data, indicating that 3D structural information is necessary for the analysis.

The novel methodology proposed here can be further extended to the structural studies of the block copolymer thin film with more complex morphologies, e.g., gyroid,

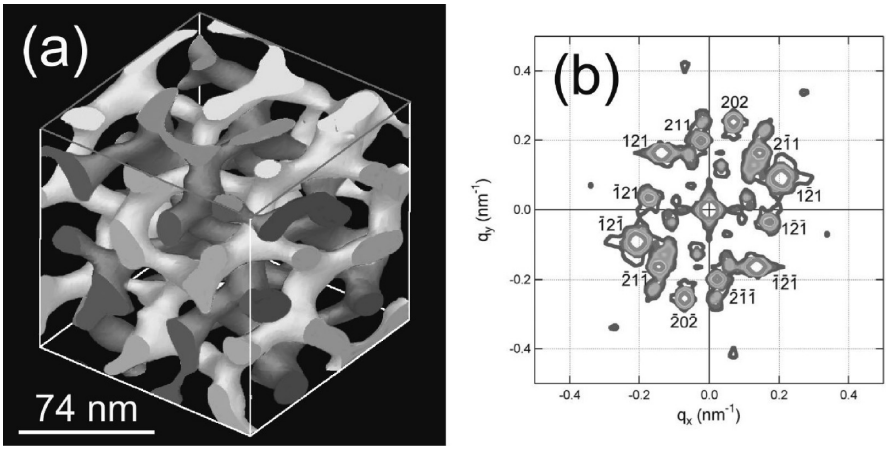

Figure 9. (a) Transmission electron microtomograph of gyroid morphology in SIS triblock copolymer. The nonintersecting light and dark channels correspond to the minority microphase (S in the SIS copolymer), while the majority (I) microphase is transparent. The edge of each cube is equal to twice the periodic length, and the top cross section is the (001) plane. Forty-nine digital images were acquired at a resolution of 2.1 nm/pixel and tilt angles ranging from $+60°$ to $-60°$ in 2.5° increments. A detailed experimental procedure can be found elsewhere.[60] (b) Fourier transformation of 3D structure of SIS triblock copolymer at $q_z = 0$. Numbers at some diffraction spots indicate the Miller indices of the gyroid structure.

perforated layers, etc. It can also be extended to off-specular scattering data[70,73−76] as well as specular scattering data, i.e., reflectivity data, because the 3D volume data obtained from TEMT provide not only depth information but also in-plane structural information. The combination of 3D real- and Fourier-space methods will be useful for morphological studies in general, and hence, it is expected to become popular in the future.

4. Some Examples and Perspective of Polymer Nanostructure Studies Using TEMT

TEMT is an ideal tool for characterization of polymer nanostructures, and as such, it has proven useful for providing high-resolution 3D information on a variety of polymeric structures, e.g., block copolymer nanoscale microphase-separated structures,[45,56,58,60,77−79] nanocomposite materials,[80,81] carbon black/natural rubber composites,[62] etc. Some of these studies provided not only *clear* 3D pictures but also *quantitative* structural information. In what follows, we briefly show some examples of structural studies carried out using TEMT to show possible future applications of the methods in polymer science.

A. Microphase-Separated Morphologies of Block Copolymers: Morphological Studies. Following the classic study carried out by Spontak et al.,[56] a couple of morphological studies were carried out in the 1990s.[57−59] The numbers of studies using TEMT on block copolymers are increasing rapidly, especially in the past couple of years. This technique has been mainly used for structural investigations due to its 3D visualization capability.[18,77,78,82−90]

Figure 9a shows one of the representative reconstructed 3D images of the microphase-separated structure showing the gyroid (G) morphology. It is formed in poly(styrene-*block*-isoprene-*block*-styrene) (SIS) triblock copolymer. The light and dark channel networks evident in Figure 9a both represent the polystyrene (S) microphase. They are shaded differently to show that the two S channel networks do not intersect. For the sake of clarity in this figure, the isoprene (I) microphase is transparent. We note here that an excellent review paper has been published[91] on the topic of "ordered network mesostructures" such as the SIS triblock terpolymer described in this section, for which TEMT would be the ideal characterization tool.

The single-grain structure factor can be obtained by the Fourier transformation of the 3D structures once a single G grain is extracted. Needless to say, the structure factor corresponds to the "(small-angle X-ray) scattering pattern" of the morphology. Figure 9b shows that such a structure factor at q_z is zero (q is the wavenumber). Several diffraction spots are clearly observed, a crystallographic analysis of which identifies the microphase-separated structure is G. Besides such morphological characterization in the Fourier space, geometrical and topological features of the complex G morphology, e.g., average coordination number of the S network, Euler characteristics,[92] surface curvature,[60] etc., have been measured from the 3D structures. Surface curvature is particularly important because it is related to the packing frustration of the blocks inside the microdomain[93] and, thus, the stability of the 3D morphology of the copolymer. We note here that these structural parameters can be *directly* obtained only from the 3D images. In addition, the analysis of the 3D volume data of the SIS copolymer reveals many defects, e.g., the disconnection of polystyrene (PS) networks, multiple branches at junctions other than 3 (the coordination number of the G nanostructure is 3) [a 3D movie is available in the Supporting Information]. One of the advantages of 3D data is that nanostructures can be virtually observed from inside.

Another interesting example of visualizing complex 3D morphology by TEMT is the double-helical structure of polystyrene-*block*-polybutadiene-*block*-poly(methyl methacrylate) triblock terpolymer (SBM).[61] Since the discovery of the double-helical structure of DNA,[94] the helix has been an attractive subject for investigations of molecular structure.[95−99] In materials science, numerous studies have investigated the artificial creation and control of helical structures. Because of their sophisticated self-assembling capabilities, block copolymers have been used to mimic the well-known biological architecture, the helix.[95−97,100]

Figure 10 shows TEM micrographs of the SBM triblock terpolymer, in which the dark gray regions correspond to the OsO_4-stained PB microdomains. The white and light gray regions are the poly(methyl methacrylate) (PMMA) and PS microdomains, respectively. The TEM images reveal that the PS cylinders along with the PB helical microdomains are hexagonally packed in the PMMA matrix. The PS cylindrical microdomains are not completely covered by the PB microdomains, as shown in Figure 10a. Although the nanostructure of the SBM triblock terpolymer is quite interesting, the 2D projection of the 3D structure *did not* provide adequate structural information.

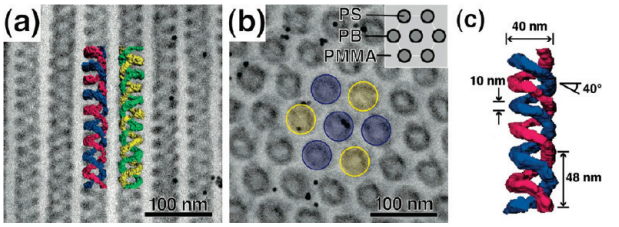

Figure 10. TEM micrographs of SBM triblock terpolymer showing its two representative morphology. OsO_4-stained PB microdomains appear in black. (a, b) Two representative morphologies of SBM terpolymer. As schematically shown in the inset of (b), the PS cylinders with the PB helical microdomains are hexagonally packed in the PMMA matrix. 3D structures of the double-helical structures are shown on the top of the TEM image in (a). Left- and right-handed double-helical structures are found and are shown by blue-red and green-yellow helixes, respectively. The spatial arrangements of the left- and right-handed helixes are also shown in (b) by blue and yellow circles, respectively. (c) Structural dimensions, e.g., pitch of helix, *d*, diameter of helix, *D*, etc. The TEM and TEMT 3D observations were carried out using a JEM-2200FS (JEOL Co., Ltd., Japan) operated at 200 kV. A series of TEM images were acquired at tilt angles ranging from ±75° at an angular interval of 1°. The experimental details can be found elsewhere.[61]

Both left- and right-handed double-helical structures could be clearly visualized by TEMT (Figure 10a). Contrary to the previous report on the same triblock copolymer by Krappe et al.,[95] it was found that the SBM triblock terpolymer has a simple "double"-helical structure and not a four-stranded (i.e., "double double") helical structure. Interestingly, the number of left- and right-handed helical structures was the same. Although the structural order in terms of the helical sense appears to be random, at least at first glance, it is likely that an adjacent pair takes opposing helical configurations (see Figure 10a). Such detailed but important features of the helical structures can be obtained only by TEMT. It appears that with helical "mesoscale" structures are becoming popular,[99−102] TEMT will be one of the essential tools for studying the helical morphology as well as complex microphase-separated structures in general.

B. Microphase-Separated Morphologies of Block Copolymers: Dynamical Aspects. The main advantage of TEMT is that it does not require any prerequisite assumptions in acquiring 3D images. The two examples described in the previous section demonstrate that TEMT is one of the most powerful methods to investigate "static" polymer nanostructures, especially the complex ones. Unlike other microscopy techniques such as light microscopy, the samples for TEMT are microtomed; hence, this technique is limited to the observation of the fixed 3D morphologies. In some cases, however, dynamical processes of polymer nanostructures may be studied from 3D "snapshots".

It is well-known that block copolymers undergo order−order phase transitions (OOTs), which often exhibit an epitaxial relationship between the morphology of two phases.[103−110] One of the extensively studied examples is the phase transition from or to the G structure, which is more intriguing than the others due to the structural complexity of the G phase.

Figure 11 shows a TEMT image and digitally sliced images of the gyroid (G)/hexagonally packed cylinder (HEX) transitional structure of a poly(styrene-*block*-isoprene) (SI) block copolymer.[111] In the 3D image (Figure 11a), only the PS domain is shown, and this hexahedral image is obtained from the rectangular box area in the TEM image shown in Figure 11b. The dimension of the hexahedron is 400, 200, and 80 nm (*X*, *Y*, *Z*). Here, *Z* is the direction of incident electron beam, and *X*−*Z* is the film plane (i.e., substrate surface). Figure 11b clearly shows the grain boundary region of the coexisting G and HEX phases. HEX cylinders are oriented along the *X*-axis, while the G phase shows the $\{111\}_G$ plane characterized by the wagon-wheel-shaped structure. For deeper understanding of the 3D nanostructure of the coexisting morphology of G and HEX, several digitally sliced images are obtained for the cross section of the hexahedron. Figure 11e shows an image of the HEX grain perpendicular to the cylinder axis, while Figure 11f shows an image of $\{220\}_G$, which is orthogonal to both $\{121\}_G$ and $\{111\}_G$.

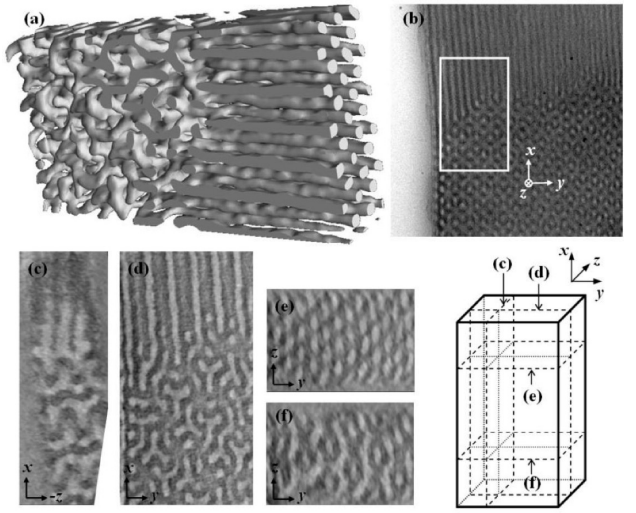

Figure 11. (a) 3D reconstructed image of coexisting structure of G and HEX. The dimension of the hexahedron is 400 nm × 200 nm × 80 nm (*X*, *Y*, *Z*). Only the PS domain is shown. (b) TEM image of sample region from which 3D image was reconstructed (boxed area). (c−f) Images of cross section illustrated in hexahedron. Polyisoprene (PI) block was stained with OsO_4 and appears darker. The TEM and TEMT 3D observations were carried out using a JEM-2200FS (JEOL Co., Ltd., Japan) operated at 200 kV whose details can be found elsewhere.[111]

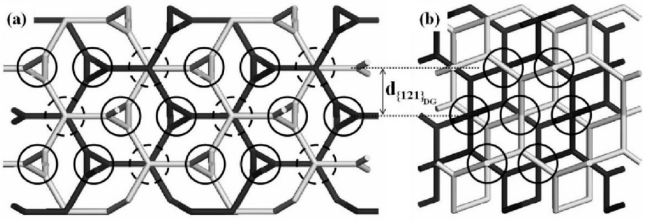

Figure 12. (a) Simulated projection along $\langle 111\rangle_G$. The two single gyroids are expressed by different gray tones. The loci of the cylinder axis are indicated by circles. There are two different types of loci, as indicated by solid and dotted circles. (b) Simulated projection along $\langle 220\rangle_G$. The loci of the cylinder axis are indicated by circles. In this $\langle 220\rangle_G \rightarrow$ cylinder axis mechanism, all loci are equivalent.

These results indicate that the HEX cylinder axis is perpendicular to $\{220\}_G$ and parallel to both $\{121\}_G$ and $\{111\}_G$. Figures 11c,d show the images consistent with this result. Figure 11c shows the coexisting $\{10\}_{HEX}$ and $\{121\}_G$. Figure 11d shows a magnified version of the image in Figure 11b. The former clearly shows coexisting $\{11\}_{HEX}$ and $\{111\}_G$ since it is a digitally sliced image. Therefore, it is unambiguously confirmed that $\{121\}_G$ and $\{111\}_G$ were respectively converted to $\{10\}_{HEX}$ and $\{11\}_{HEX}$.

Matsen has reported on how the phase transition between G and HEX occurs.[106] According to his proposal,

the $\langle 111\rangle_G$ axis is converted to the cylinder axis of HEX. As illustrated in Figure 12a, the projection along the $\langle 111\rangle_G$ direction has 3-fold symmetry, and the loci corresponding to the HEX cylinder axes are indicated by small circles. The loci are not structurally uniform but are of two different types, as indicated by solid and dotted circles. At the loci indicated by dotted circles, tripodal skeletons of two single gyroids have to be connected to form a HEX cylinder. An appropriate mechanism for this conversion from G to HEX has been proposed by Matsen.[106] On the other hand, in the new transitional structure observed in this section, the HEX cylinder is formed along the $\langle 220\rangle_G$ direction. The symmetry of the $\{220\}_G$ projection is slightly distorted from the right hexagon, as shown in Figure 12b, where the loci of cylinders are indicated by circles. In contrast to the $\langle 111\rangle_G \rightarrow$ cylinder axis mechanism,[106,110,112] all loci are equivalent, and the cylinder axis would grow connecting two single gyroid skeletons.[111] Even though the hexagon is distorted, the $\{121\}_G$ plane gets to be converted to the $\{10\}_{HEX}$ plane without perturbation. This type of epitaxial transition path has not been observed in previous studies.

One of the distinct features of the above-mentioned example is its thin film structure. The surface interactions of block copolymers may play more important role in the thin film OOTs rather than in the bulk OOTs. The phase transition behaviors in thin films as compared to those of bulk have been reported earlier. Park et al. have reported that in the phase transition of HPL (hexagonally perforated layer) → G HPL layers are converted to $\{121\}_G$ in thin films,[109] while such an orderly transition is not observed in shear-oriented bulk.[104,105] Similarly, Mareau et al. have reported that in the G/HPL grain boundary structure in bulk HPL layers are connected to $\{111\}_G$,[113] which is again not compatible with the epitaxial relationship between the HPL layers and $\{121\}_G$ found in thin films.[109] Thus, the OOTs in block copolymers have to be further investigated, and TEMT is an essential tool for the investigation because it provides not only the epitaxial relations between the prexisting and newly formed microdomains but also mechanisms of rearrangement of microdomains during the OOTs.[111,112,114]

C. Single Chain Conformation Inside Microphase-Separated Morphologies. As described in section 4.A, block copolymers have a tendency to self-assemble, forming films with highly periodic nanoscale morphologies.[115] The subchains of block copolymers are packed in the microdomains with their chemical junctions presumably placed at the interface. Because of such topological constraints, the subchains are sometimes awkwardly accommodated in the nanodomains ("packing frustration").[92] The balance between the interaction (enthalpy) and frustration of the subchains (entropy) determines the final morphologies. Because the packing frustration arises from deviation in the chains from their preferred conformation, scientists plan to devise methods to visualize the chain conformation not only in bulk[116−121] but also in restricted dimensions.[122−124]

Small-angle neutron (or X-ray) scattering has been used to evaluate the gyration radius R_g of the subchains in lamellar-forming block copolymers.[116−119] The results of these evaluations have shown that the lateral interpenetration of the subchains is smaller than the interpenetration normal to the interface. The obtained R_g is, however, the averaged value, while R_g is intrinsically a local quantity. A simulation technique has been *independently* used for investigating the conformation of specific chains in nanodomains.[125−127] For example, Aoyagi and co-workers[126] have estimated the ratio of bridge to loop conformations in the lamellar domains of an ABA-type triblock copolymer

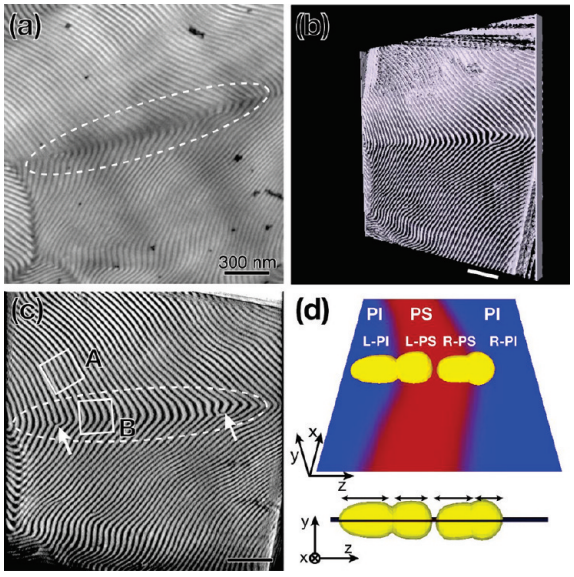

Figure 13. Images obtained by (a) TEM and (b, c) TEMT. The scale bars in each figure indicate 300 nm. The white broken lines in (a) and (c) show the boundary region between two grains, while the squares in (c) indicate the regions studied using SCF simulations. (d) Single chain distribution in bent lamellar domains. The density of the PS segments projected on the $X-Z$ plane is shown by color gradation, and the distribution of single chains, $\phi_{single}(\mathbf{r})$, is shown by the yellow contour surfaces. A JEM-1010 transmission electron microscope (JEOL, Co., Ltd., Japan) at an accelerating voltage of 100 kV. The tilt angles ranging from −60° to +60° in 2° increments. Details of experiments as well as computer simulations can be found in the literature.[132]

using the self-consistent-field (SCF)[128−130] and the coarse-grained molecular dynamics (CGMD)[125,131] simulations. The success of these studies indicates that the collaboration between experiments and SCF simulations can be further improved.

Figure 13a shows a TEM micrograph, and Figures 13b,c show the images obtained by TEMT. In the TEMT images, a grain boundary and a lamellar morphology of SI block copolymer are clearly observed. The two cubes, A and B, shown in Figure 13c indicate the regions studied using the 3D SCF simulations. The flat lamella (A) corresponds to the equilibrium lamellar morphology, while the bent lamella (B) corresponds to the grain boundary. The experimentally obtained 3D interface is used as the "boundary condition" for the SCF simulations in order to estimate the chain conformation of subchains.[132] Detailed protocols of the SCF simulations and 3D TEMT structural data can be found elsewhere.[132] R_g is calculated using the segment distribution $\phi_{single}(\mathbf{r})$ in the flat lamellar interface and is consistent with the previous theoretical[128,133] and experimental[118] results.

Figure 13d shows the result of the total segment density distribution of the PS subchain in the bent lamellar interface. The total density is shown by the color gradation on the $X-Z$ plane. In order to schematically show the "shape" of the PS subchain, the isodensity surface corresponding to a certain $\phi_{single}(\mathbf{r})$ is shown as a yellow surface in the figure. We show two chains whose junctions are fixed at the outer (right) and the inner (left) interfaces of the PS nanodomain. Intriguingly, the PS subchain of the right-hand side chain (R-PS) is more stretched than that of the left-hand side (L-PS). This is due to the effect of the curvature of the interface. In the bent region, the chains are subjected to a stretching or compression force arising from the extra gradient of the SCF due to the interfacial curvature, which is caused by incompressibility. This indicates that the local stress in the nanoregion of

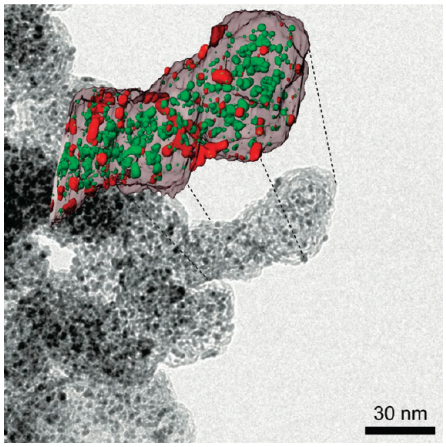

Figure 14. TEM micrograph of polymer fuel cell electrode (background). The small dots are Pt particles on a carbon black substrate, "Ketjenblack" (supplied by Tanaka Kikinzoku Kogyo K. K.). The electrode does not contain an ionomer. The electrode is rotated inside TEMT up to ±90° with 1° increments on a JEM-2200FS (JEOL Co., Ltd., Japan) operated at 200 kV. 181 TEM projections are recorded, which are used for the 3D reconstruction. The same experimental protocol described in the ref 139 was used. The inset shows the 3D image of the tip part of electrode, where Pt catalysts inside and on the surface of Ketjenblack are shown in green and red, respectively. The dashed line shows the correspondence between the TEM and TEMT images.

the deformed structures can be illustrated using the stretching or compression conformation of the single chain. Thus, we can analyze the conformation of a subchain localized at a particular point in the real nanodomain by combining TEMT and computer simulation. We expect that this method will aid in understanding self-assembled structures and improving material properties in the future.

D. TEMT for Energy Applications. Finally, we show that TEMT is also essential for energy applications. Polymer-based fuel cells and nanostructured polymer solar cells are environment-friendly next-generation power sources. Such energy sources with significantly enhanced energy output and durability are in high demand, especially for automotive applications. However, the performance loss of the fuel cells during operation prevents their practical application. Therefore, degradation mechanisms of fuel cells has to be intensively studied. The polymer fuel cell electrode (PFCE), consisting of platinum particles or platinum alloy particles (Pt catalysts) supported on graphite carbon particles and proton-conducting ionomer binder, is one of the most important components[134] of fuel cells and may be a source of the degradation. The detailed characterization of PFCEs before and after the operation is significant in order to understand the degradation mechanisms for further improving of the durability of the cells.

The degradation of cell performance is believed to be related to the CO adsorption on active catalysts at the anode.[135,136] The size of Pt catalyst particles is also believed to increase after the operation of fuel cells.[137] The increase in the size of Pt catalyst particles results in the reduction of the active surface area of the catalyst, which affects the reaction kinetics and ultimately degrades the cell performance. TEM has been one of the most popular techniques used to characterize the morphology of fuel cell catalysts in terms of not only the catalyst particle size but also their shape and distribution.[137,138] However, particles often overlap along the optical axis of the microscope, which prevents the accurate evaluation of the structural information.

Figure 14 shows a TEM micrograph of a PFCE. The light gray part and dots indicate the carbon substrate ("Ketjenblack") and Pt catalysts, respectively. In the figure, a TEMT reconstructed image of the part of the PFCE is also displayed. The spatial distribution of Pt catalysts with respect to Ketjenblack is clearly shown. The experimental technique described in section 3.A, i.e., ±90° rotation experiment, is employed in this case. Because the diameter of the Pt particles is ca. 2−3 nm, high-resolution 3D imaging (below 1 nm resolution) is required. The green and red dots indicate Pt catalyst particles located *inside* and *on the surface of* Ketjenblack, respectively. Almost 70% of the Pt catalyst particles were found to be inside Ketjenblack. This finding is in sharp contrast with our previously examined PFCE with a different type of carbon substrate called "Vulcan", in which all the Pt catalyst particles were located only on the surface of the carbon substrate.[139]

It is commonly believed that Pt catalysts on carbon substrates contribute to the electrochemical reaction because it takes place where the Pt catalysts and ionomer meet. In this case, the Pt particles inside the graphite carbon substrate, if any, should not work due to the absence of the ionomer. However, the PFCE made of Ketjenblack examined here has superior performance as compared to the one with Vulcan (the content of Pt catalysts is the same for both electrodes). In addition, it appears that the former has longer durability than the latter. In a separate low-resolution elementally specific TEMT experiment using fluorine as the target element (the ionomer containes F), it is shown that the ionomer exists inside Ketjenblack. Thus, the internal Pt catalysts do contribute to the electrochemical reaction and the PFCE with Ketjenblack substrate may show longer durability probably because the Pt catalysts inside the substrate may be protected. Although further experiments are necessary to prove these speculations and clarify the degradation mechanisms of the PFCE, it is obvious that TEMT provids considerably better structural information than conventional TEM. In another energy-related device, i.e., polymer solar cells, the photoactive layer is made of at least two functional materials that form nanoscale interpenetrating phases with specific functionalities. TEMT is also used to investigate interpenetrating 3D structures. Researchers are trying to optimize the photoactivity of solar cells.[90,140,141]

5. Summary

This Perspective summarizes the recent advances and perspectives in three-dimensional (3D) microscopy, especially transmission electron microtomography (TEMT).[45,46] TEMT is based on tomography and transmission electron microscopy (TEM). TEMT has been proven to be quite useful and powerful in the characterization of polymer nanostructures. As described in section 3, TEMT can be used for *truly quantitative* measurements by introducing a "needle-type" specimen for ±90° rotation.[49] This is a breakthrough in TEMT because the method has suffered from drawbacks such insufficient as rotation range of specimens and low anisotropic image resolution for nearly 20 years, since its introduction in 1988.[56] Moreover, a micrometer thick specimens can be observed with a resolution of few nanometers, which enables us to cover *hierarchical* polymer nanostructures ranging from a few nanometers up to several hundred nanometers. It has also been shown that the combination of TEMT and scattering methods provides considerably better structural information than using just one of these methods. In section 3.C, a featureless reflectivity profile of a cylinder-forming block copolymer thin film was clearly explained with the aid of 3D structures obtained by TEMT. As the polymer nanostructures become more and more complex, such a combinatorial approach using both *real*- and the *Fourier-space* methods, i.e., TEMT and scattering, will be very important.

From the 3D volume data array obtained by TEMT, some basic structural parameters, e.g., the volume fraction and the interfacial area per unit volume of 3D objects, can be *directly* and relatively easily measured. These structural parameters are basic, but they have been so far inferred from 2D images and, therefore, were possibly inaccurate. The characteristic length, if any, readily measured by using a scattering technique, can also be estimated by taking the Fourier transform of 3D images. A new set of structural parameters, e.g., interfacial curvature, connectivity of network microdomains, etc., can also be measured. We would like to emphasize that these geometrical parameters cannot be evaluated by any other (conventional) experimental technique besides 3D microscopy.[45] Further, the size, distribution, and orientation of platelike filers, e.g., montmorillonite, in nonocomposite materials can be quantitatively obtained.[80,114]

For the application of TEMT to polymer nanostructures, we employed block copolymer nanostructures as one of the representatives, as described in section 4. The double-helical morphology of an ABC-type triblock terpolymer as well as the bicontinuous morphology of an ABA-type block copolymer could be clearly imaged. The space group of the bicontinuous morphology was a controversial issue in the early 1990s, but it has been characterized now by using 3D images.[59,91] The helical sense and pitch, the essential structural parameters to characterize helical structures, may be most efficiently measured by using TEMT.[61]

From 3D structures, it is possible to investigate the essential aspects of block copolymer self-assembling processes. The order−order transition (OOT) in a block copolymer from gyroid to cylinder morphologies was studied by TEMT. The obtained 3D structures at the boundary between the preexisting gyroids and the newly formed cylindrical microdomains showed epitaxial relation, close examination of which showed the transition mechanism of the OOT. Morphological studies of thin films are another interesting area due to their wide range of applications in nanotechnology.[142] For example, an unusual thickness-induced morphological transition from cylinders to spheres in a cylinder-forming block copolymer (in the bulk) was found by TEMT.[67] Such morphological change could be overlooked only if the surface morphology of the thin film were observed by AFM. Another essential feature of the block copolymer self-assembly, i.e., how the blocks are accommodated inside microdomains, may be visualized by combining TEMT and advanced computer simulations, as described in section 4.C. TEMT will play an important role not only in morphological studies but also in energy applications such as the next-generation cells for improving their designs and durability.

Finally, we will further develop TEMT, an excellent 3D visualization tool that can be used in nano- and mesoscale ranges, so that we can observe specimens under various "environments", e.g., under atmospheric pressure, indentation, or stretching, etc., in three dimensions. Adding the *fourth* dimension, time, is also important in 3D imaging, which we hope to deal with in the future.

Acknowledgment. We thank Prof. T. Chang and Dr. H.-W. Park (Pohang University of Science and Technology, Korea), Prof. Dr. V. Abetz (Institute of Polymer Research, GKSS Research Centre Geesthacht GmbH), Prof. S. Nakahama (Tokyo Institute of Technology), Prof. K. Tanaka (Kyushu University), Dr. H. Morita (Advanced Industrial Science and Technology), Mr. T. Mihara (Toray Industries Inc.), and Dr. K. Niihara, Messrs. H. Sugimori, and T. Tanaka (Kyoto Institute of Technology) for their support, collaboration, and useful discussions. We also thank Dr. N. Kawase and Dr. M. Kato (Nitto Analytical Techno-Center Co., Ltd.) for their helpful discussions and their assistance in TEMT experiments (section 3.A). We are grateful to Dr. S. Motoki, Dr. T. Kaneko, and Dr. T. Aoyama and Messrs. H. Nishioka, Y. Ohkura, and Y. Kondo (JEOL Ltd.) for their assistance in conducting the STEMT experiments (section 3.B). Messrs. T. Ito, U. Matsuwaki, and Y. Otsuka (Toray Research Center Inc.) are gratefully acknowledged for their useful discussions and assistance in carrying out experiments (section 4.D). We are grateful to NEDO for support through the Japanese National Project "Nano-Structured Polymer Project" by the Ministry of Economy, Trade and Industry. This study was also partly supported by NEDO under the Polymer Electrolyte Fuel Cell Program "Strategic Development of PEFC Technologies for Practical Application/Development of Technology for Next-Generation Fuel Cells". H.J. gratefully acknowledges the financial support received through Grants-in-Aid No. 19031016, No. 21015017, and No. 21241030 from the Ministry of Education, Science, Sports and Culture.

Supporting Information Available: An AVI videos showing the "fly-through" of bicontinuous morphologies of the SIS triblock copolymer (Figure 9). This material is available free of charge via the Internet at http://pubs.acs.org.

References and Notes

(1) Hashimoto, T. Structure of Polymer Blends. In *Structure and Properties of Polymers*; Cahn, R. W., Haasen, P., Kramer, E. J., Eds.; VCH: Weinheim, 1993; Vol. *12*.
(2) Jinnai, H.; Nishikawa, Y.; Koga, T.; Hashimoto, T. *Macromolecules* **1995**, *28*, 4782–4784.
(3) Jinnai, H.; Koga, T.; Nishikawa, Y.; Hashimoto, T.; Hyde, S. T. *Phys. Rev. Lett.* **1997**, *78*, 2248–2251.
(4) Lopez-Barron, C. R.; Macosko, C. W. *Langmuir* **2009**, *25*, 9392–9404.
(5) Bates, F. S.; Fredrickson, G. H. *Phys. Today* **1999**, *52*, 32–38.
(6) Abetz, V.; Simon, P. F. W. *Adv. Polym. Sci.* **2005**, *189*, 125–212.
(7) Kawasumi, M.; Hasegawa, N.; Kato, M.; Usuki, A.; Okada, A. *Macromolecules* **1997**, *30*, 6333–6338.
(8) Maiti, P.; Nam, P. H.; Okamoto, M.; Hasegawa, N.; Usuki, A. *Macromolecules* **2002**, *35*, 2042–2049.
(9) Busfield, J. J. C.; Deeprasertkul, C.; Thomas, A. G. *Polymer* **2000**, *41*, 9219–9225.
(10) Tsunoda, K.; Busfield, J. J. C.; Davies, C. K. L.; Thomas, A. G. *J. Mater. Sci.* **2000**, *35*, 5187–5198.
(11) Yamaguchi, K.; Busfield, J. J. C.; Thomas, A. G. *J. Polym. Sci., Part B: Polym. Phys.* **2003**, *41*, 2079–2167.
(12) Busfield, J. J. C.; Thomas, A. G.; Yamaguchi, K. *J. Polym. Sci., Part B: Polym. Phys.* **2003**, *42*, 2161–2089.
(13) Hawker, C. J.; Wooley, K. L. *Science* **2005**, *309*, 1200–1205.
(14) Kamigaito, M.; Sato, K. *Macromolecules* **2008**, *41*, 269–276.
(15) Percec, V. *Nat. Chem.* **2009**, *109*, 4961–4962.
(16) Matyjaszewski, K.; Tsarevsky, N. V. *Nat. Chem.* **2009**, *1*, 276–288.
(17) Ito, M.; Ejiri, S.; Jinnai, H.; Kono, J.; Ikeda, S.; Nishida, A.; Uesugi, K.; Yagi, N.; Tanaka, M.; Hayashi, K. *J. Bone Miner. Metab.* **2003**, *21*, 287–293.
(18) Jinnai, H.; Nishikawa, Y.; Ito, M.; Smith, S. D.; Agard, D. A.; Spontak, R. J. *Adv. Mater.* **2002**, *14*, 1615–1618.
(19) Tanaka, T.; Mihara, T.; Saito, H.; Jinnai, H., manuscript in preparation.
(20) Momose, A.; Fujii, A.; Jinnai, H.; Kadowaki, H. *Macromolecules* **2005**, *38*, 7197–7200.
(21) Koizumi, S.; Yamane, Y.; Kuroki, S.; Ando, I.; Nishikawa, Y.; Jinnai, H. *J. Appl. Polym. Sci.* **2007**, *103*, 470–475.
(22) Nishino, Y.; Takahashi, Y.; Imamoto, N.; Ishikawa, T.; Maeshima, K. *Phys. Rev. Lett.* **2009**, *102*, 018101–018104.
(23) Fienup, J. R. *Appl. Opt.* **1982**, *21*, 2758–2769.
(24) Miao, J.; Charalambous, P.; Kirz, J.; Sayre, D. *Nature* **1999**, *400*, 342–344.
(25) Loos, J.; Sourty, E.; Lu, K.; Freitag, B.; Tang, D.; Wall, D. *Nano Lett.* **2009**, *9*, 1704–1708.
(26) Motoki, S.; Kaneko, T.; Aoyama, Y.; Nishioka, H.; Ohkura, Y.; Kondo, Y.; Jinnai, H., revised manuscript submitted to *J. Electron Microsc.*
(27) Dunn, D. N.; Hull, R. *Appl. Phys. Lett.* **1999**, *75*, 3414–3416.
(28) Magerle, R. *Phys. Rev. Lett.* **2000**, *85*, 2749–2752.

(29) Kato, M.; Ito, T.; Aoyama, Y.; Sawa, K.; Kaneko, T.; Kawase, N.; Jinnai, H. *J. Polym. Sci., Part B: Polym. Phys.* **2007**, *45*, 677–683.
(30) Efimov, A.; Muench, B.; Wegmann, M.; Gasser, P.; Flatt, R. *J. Microsc.* **2007**, *226*, 207–217.
(31) Bracewell, R. N. *Aust. J. Phys.* **1956**, *9*, 297.
(32) Cormack, A. M. *J. Appl. Phys.* **1963**, *34*, 2722.
(33) Hounsfield, G. N. A. *Method and Apparatus for Examination of a Body by Radiation such as X or Gamma Radiation*; The Patent Office: London, 1972.
(34) de Rosier, D. J.; Klug, A. *Nature* **1968**, *217*, 130.
(35) Hoppe, W.; Langer, R.; Knesch, G.; Poppe, C. *Naturwissenschaften* **1968**, *55*, 333.
(36) Hart, R. G. *Science* **1968**, *159*, 1464.
(37) Crowther, R. A.; DeRosier, D. J.; Klug, A. *Proc. R. Soc. London* **1970**, *A 317*, 319–340.
(38) Vainshtein, B. K. *Sov. Phys. Crystallogr.* **1970**, *15*, 781.
(39) Ramachandran, G. N.; Lakshminarayanan, A. V. *Proc. Natl. Acad. Sci. U.S.A.* **1971**, *68*, 2236.
(40) Gordon, R.; Bender, R.; Herman, G. T. *J. Theor. Biol.* **1970**, *29*, 471.
(41) Gilbert, P. *J. Theor. Biol.* **1972**, *36*, 105.
(42) Batenburg, K. J.; Bals, S.; Sijbers, J.; Kübel, C.; Midgley, P. A.; Hernandez, J. C.; Kaiser, U.; Encina, E. R.; Coronado, E. A.; Tendeloo, G. V. *Ultramicroscopy* **2009**, *109*, 730–740.
(43) Frank, J. *Electron Tomography: Three-Dimensional Imaging with the Transmission Electron Microscope*; Plenum: New York, 1992.
(44) Midgley, P. A.; Weyland, M. *Ultramicroscopy* **2003**, *96*, 413–431.
(45) Jinnai, H.; Nishikawa, Y.; Ikehara, T.; Nishi, T. *Adv. Polym. Sci.* **2004**, *170*, 115–167.
(46) Jinnai, H.; Spontak, R. J. *Polymer* **2009**, *50*, 1067–1087.
(47) Friedrich, H.; de Jongh, P. E.; Verkleij, A. J.; de Jong, K. P. *Chem. Rev.* **2009**, *109*, 1613–1629.
(48) Kaneko, T.; Nishioka, H.; Nishi, T.; Jinnai, H. *J. Electron Microsc.* **2005**, *54*, 437–444.
(49) Kawase, N.; Kato, M.; Nishioka, H.; Jinnai, H. *Ultramicroscopy* **2007**, *107*, 8–15.
(50) Sugimori, H.; Nishi, T.; Jinnai, H. *Macromolecules* **2005**, *38*, 10226–10233.
(51) Penczek, P.; Marko, M.; Buttle, K.; Frank, J. *Ultramicroscopy* **1995**, *60*, 393–410.
(52) Mastronarde, D. N. *J. Struct. Biol.* **1997**, *120*, 343–352.
(53) Barnard, D. P.; Turner, J. N.; Frank, J.; McEwen, B. F. *J. Microsc.* **1992**, *167*, 39–48.
(54) Niihara, K.; Kaneko, T.; Suzuki, T.; Sato, Y.; Nishioka, H.; Nishikawa, Y.; Nishi, T.; Jinnai, H. *Macromolecules* **2005**, *38*, 3048–3050.
(55) Crowther, R. A.; DeRosier, D. J.; Klug, A. *Proc. R. Soc. London* **1970**, *A 317*, 319–340.
(56) Spontak, R. J.; Williams, M. C.; Agard, D. A. *Polymer* **1988**, *29*, 387–395.
(57) Spontak, R. J.; Fung, J. C.; Braunfeld, M. B.; Sedat, J. W.; Agard, D. A.; Kane, L.; Smith, S. D.; Satkowski, M. M.; Ashraf, A.; Hajduk, D. A.; Gruner, S. M. *Macromolecules* **1996**, *29*, 4494–4507.
(58) Radzilowski, L. H.; Carragher, B. O.; Stupp, S. I. *Macromolecules* **1997**, *30*, 2110–2119.
(59) Laurer, J. H.; Hajduk, D. A.; Fung, J. C.; Sedat, J. W.; Smith, S. D.; Gruner, S. M.; Agard, D. A.; Spontak, R. J. *Macromolecules* **1997**, *30*, 3938–3941.
(60) Jinnai, H.; Nishikawa, Y.; Spontak, R. J.; Smith, S. D.; Agard, D. A.; Hashimoto, T. *Phys. Rev. Lett.* **2000**, *84*, 518–521.
(61) Jinnai, H.; Kaneko, T.; Matsunaga, K.; Abetz, C.; Abetz, V. *Soft Matter* **2009**, *5*, 2042–2046.
(62) Jinnai, H.; Shinbori, Y.; Kitaoka, T.; Akutagawa, K.; Mashita, N.; Nishi, T. *Macromolecules* **2007**, *40*, 6758–6764.
(63) Aoyama, K.; Takagi, T.; Miyazawa, A. *Ultramicroscopy* **2008**, *109*, 70–80.
(64) Loos, J.; Sourty, E.; Lu, K.; de With, G.; v. Bavel, S. *Macromolecules* **2009**, *42*, 2581–2586.
(65) Goldstein, J. I.; Costley, J. L.; Lorimer, G. W.; Reed, S. J. B. Quantitative X-ray analysis in the electron microscope. In *Proceedings of the 10th Annual Scanning Electron Microscope Symposium and Workshop on Materials and Component Characterization/Quality Control with the SEM/STEM*; Johari, O., Ed.; IIT Research Institute: Chicago, 1977.
(66) Aoyama, Y.; Motoki, S.; Kaneko, T.; Nishioka, H.; Ohkura, Y.; Kondo, Y.; Jinnai, H., manuscript in preparation.
(67) Niihara, K.; Matsuwaki, U.; Torikai, N.; Atarashi, H.; Tanaka, K.; Jinnai, H. *Macromolecules* **2007**, *40*, 6940–6946.
(68) Lawrence, M. C. *Macromolecules* **1997**, *30*, 2110–2119.
(69) Parratt, L. G. *Phys. Rev.* **1954**, *95*, 359–369.
(70) Russell, T. P. *Mater. Sci. Rep.* **1990**, *5*, 171–271.
(71) Karim, A.; Guo, L.; Rafailovichi, M. H.; Sokolov, J.; Peiffer, D. G.; Schwarz, S. A.; Colby, R. H.; Dozier, W. D. *J. Chem. Phys.* **1994**, *100*, 1620–1629.
(72) Knoll, A.; Tsarkova, L.; Krausch, G. *Nano Lett.* **2007**, *7*, 843–846.
(73) Pasyuk, V. L.; Lauter, H. J.; Gordeev, G. P.; Buschbaum, P. M.; Toperverg, B. P.; Jernenkov, M.; Petry, W. *Langmuir* **2003**, *19*, 7783–7788.
(74) Lee, B.; Park, I.; Yoon, J.; Park, S.; Kim, J.; Kim, K.; Chang, T.; Ree, M. *Macromolecules* **2005**, *38*, 4311–4323.
(75) Wang, J.; Leiston-Belanger, J. M.; Sievert, J. D.; Russell, T. P. *Macromolecules* **2006**, *39*, 8487–8491.
(76) Buschbaum, P. M.; Maurer, E.; Bauer, E.; Cabitt, R. *Langmuir* **2006**, *22*, 9295–9303.
(77) Yamauchi, K.; Takahashi, K.; Hasegawa, H.; Iatrou, H.; Hadjichristidis, N.; Kaneko, T.; Nishikawa, Y.; Jinnai, H.; Matsui, T.; Nishioka, H.; Shimizu, M.; Furukawa, H. *Macromolecules* **2003**, *36*, 6962–6966.
(78) Wilder, E. A.; Braunfeld, M. B.; Jinnai, H.; Hall, C. K.; Agard, D. A.; Spontak, R. J. *J. Phys. Chem. B* **2003**, *107*, 11633–11642.
(79) Dobriyal, P.; Xiang, H.; Matsunaga, K.; Chen, J.-T.; Jinnai, H.; Russell, T. P. *Macromolecules* **2009**, *42*, 9082–9088.
(80) Nishioka, H.; Niihara, K.; Kaneko, T.; Yamanaka, J.; Inoue, T.; Nishi, T.; Jinnai, H. *Compos. Interfaces* **2006**, *13*, 589–603.
(81) Zhao, Y.; Thorkelsson, K.; Mastroianni, A. J.; Schilling, T.; Luther, J. M.; Rancatore, B. J.; Matsunaga, K.; Jinnai, H.; Wu, Y.; Poulsen, D.; Fréchet, J. M. J.; Alivisatos, A. P.; Xu, T. *Nat. Mater.* **2009**, *8*, 979–985.
(82) Xu, T.; Zvelindovsky, A. V.; Sevink, G. J. A.; Lyakhova, K. S.; Jinnai, H.; Russell, T. P. *Macromolecules* **2005**, *38*, 10788–10798.
(83) Jinnai, H.; Sawa, K.; Nishi, T. *Macromolecules* **2006**, *39*, 5815–5819.
(84) Jinnai, H.; Hasegawa, H.; Nishikawa, Y.; Sevink, G. J. A.; Braunfeld, M. B.; Agard, D. A.; Spontak, R. J. *Macromol. Rapid Commun.* **2006**, *27*, 1424–1429.
(85) Jinnai, H.; Yasuda, K.; Nishi, T. *Macromol. Symp.* **2006**, *245−246*, 170–174.
(86) Kaneko, T.; Suda, K.; Satoh, K.; Kamigaito, M.; Kato, T.; Ono, T.; Nakamura, E.; Nishi, T.; Jinnai, H. *Macromol. Symp.* **2006**, *242*, 80–86.
(87) Park, H.-W.; Im, K.; Chung, B.; Ree, M.; Chang, T.; Sawa, K.; Jinnai, H. *Macromolecules* **2007**, *40*, 2603–2605.
(88) Miura, Y.; Kaneko, T.; Satoh, K.; Kamigaito, M.; Jinnai, H.; Okamoto, Y. *Chem.—Asian J.* **2007**, *2*, 662–672.
(89) Chen, Y.; Du, J.; Xiong, M.; Guo, H.; Jinnai, H.; Kaneko, T. *Macromolecules* **2007**, *40*, 4389–4392.
(90) Yang, X.; Loos, J. *Macromolecules* **2007**, *40*, 1353–1362.
(91) Meuler, A. J.; Hillmyer, M. A.; Bates, F. S. *Macromolecules* **2009**, *42*, 7221–7250.
(92) Jinnai, H.; Kajihara, T.; Watashiba, H.; Nishikawa, Y.; Spontak, R. J. *Phys. Rev. E* **2001**, *64*, 010803(R)−010806(R), 069903(E).
(93) Matsen, M. W.; Bates, F. S. *Macromolecules* **1996**, *29*, 7641–7644.
(94) Watson, J. D.; Crick, F. H. *Nature* **1953**, *171*, 737.
(95) Krappe, U.; Stadler, R.; Voigt-Martin, I. *Macromolecules* **1995**, *28*, 4558.
(96) Cornelissen, J.; Fischer, M.; Sommerdijk, N.; Nolte, R. J. *Science* **1998**, *280*, 1427.
(97) Ho, R.-M.; Chiang, Y.-W.; Tsai, C.-C.; Lin, C.-C.; Ko, B.-T.; Huang, B.-H. *J. Am. Chem. Soc.* **2004**, *126*, 2704.
(98) Kloninger, C.; Rehahn, M. *Macromol. Chem. Phys.* **2007**, *208*, 833.
(99) Zhong, S.; Cui, H.; Chen, Z.; Wooley, K. L.; Pochan, D. J. *Soft Matter* **2008**, *4*, 647.
(100) Tseng, E.-H.; Chen, C.-K.; Chiang, Y.-W.; Ho, R.-M.; Akasaka, S.; Hasegawa, H. *J. Am. Chem. Soc.* **2009**, *50*, 1067.
(101) Wang, Y.; Qin, Y.; Berger, A.; Yau, E.; He, C.; Zhang, L.; Gösele, U.; Knez, M.; Steinhart, M. *Adv. Mater.* **2009**, *21*, 1–4.
(102) Dupont, J.; Liu, G.; Niihara, K.; Kimoto, R.; Jinnai, H. *Angew. Chem., Int. Ed.* **2009**, *48*, 6144–6147.

(103) Schulz, M. F.; Bates, F. S.; Almdal, K.; Mortensen, K. *Phys. Rev. Lett.* **1994**, *73*, 86–89.
(104) Zhao, J.; Majumdar, B.; Schulz, M. F.; Bates, F. S.; Almdal, K.; Mortensen, K.; Hajduk, D. A.; Gruner, S. M. *Macromolecules* **1996**, *29*, 1204–1215.
(105) Vigild, M. E.; Almdal, K.; Mortensen, K.; Hamley, I. W.; Fairclough, J. P. A.; Ryan, A. J. *Macromolecules* **1998**, *31*, 5702–5716.
(106) Matsen, M. W. *Phys. Rev. Lett.* **1998**, *80*, 4470–4473.
(107) Kimishima, K.; Koga, T.; Hashimoto, T. *Macromolecules* **2000**, *33*, 968–977.
(108) Wang, C.-Y.; Lodge, T. P. *Macromolecules* **2002**, *35*, 6997–7006.
(109) Park, I.; Lee, B.; Ryu, J.; Im, K.; Yoon, J.; Ree, M.; Chang, T. *Macromolecules* **2005**, *38*, 10532–10536.
(110) Honda, T.; Kawakatsu, T. *Macromolecules* **2006**, *39*, 2340–2349.
(111) Park, H.-W.; Jung, J.; Chang, T.; Matsunaga, K.; Jinnai, H. *J. Am. Chem. Soc.* **2009**, *131*, 46–47.
(112) Sugimori, H.; Niihara, K.; Kaneko, T.; Miyoshi, W.; Jinnai, H. *Prog. Theor. Phys. Suppl.* **2008**, *175*, 166–173.
(113) Mareau, V. H.; Akasaka, S.; Osaka, T.; Hasegawa, H. *Macromolecules* **2007**, *40*, 9032–9039.
(114) Dohi, H.; Kimura, H.; Kotani, M.; Kaneko, T.; Kitaoka, T.; Nishi, T.; Jinnai, H. *Polym. J.* **2007**, *39*, 749–758.
(115) Thomas, E. L.; Anderson, D. M.; Henkee, C. S.; Hoffman, D. *Nature* **1988**, *334*, 598–601.
(116) Hadziioannou, G.; Picot, C.; Skoukios, A.; Ionescu, M. L.; Mathis, A.; Duplessix, R.; Gallot, Y.; Lingelser, J. P. *Macromolecules* **1982**, *15*, 263–271.
(117) Bates, F. S.; Berney, C. V.; Cohen, R. D.; Wignall, G. D. *Polymer* **1983**, *24*, 519–524.
(118) Hasegawa, H.; Hashimoto, T.; Kawai, H.; Lodge, T. P.; Amis, E. J.; Glinka, C. J.; Han, C. C. *Macromolecules* **1985**, *18*, 67–78.
(119) Hasegawa, H.; Tanaka, H.; Hashimoto, T.; Han, C. C. *Macromolecules* **1987**, *20*, 2120–2127.
(120) Matsushita, Y.; Torikai, N.; Mogi, Y.; Noda, I.; Han, C. C. *Macromolecules* **1994**, *27*, 4566–4569.
(121) Yang, J.; Sekine, R.; Aoki, H.; Ito, S. *Macromolecules* **2007**, *40*, 7573–7580.
(122) Mayes, A. M.; Russell, T. P.; Satija, S. K.; Majkrzak, C. F. *Macromolecules* **1992**, *25*, 6523–6531.
(123) Tamai, Y.; Sekine, R.; Aoki, H.; Ito, S. *Macromolecules* **2009**, *42*, 4224–4229.
(124) Sekine, R.; Aoki, H.; Ito, S. *J. Phys. Chem. B* **2009**, *113*, 7095–7100.
(125) Kremer, K.; Grest, G. S. *J. Chem. Phys.* **1990**, *92*, 5057–5086.
(126) Aoyagi, T.; Honda, T.; Doi, M. *J. Chem. Phys.* **2002**, *117*, 8153–8161.
(127) Torikai, N.; Noda, I.; Karim, A.; Satija, A. K.; Han, C. C.; Matsushita, Y.; Kawakatsu, T. *Macromolecules* **1997**, *30*, 2907–2914.
(128) Helfand, E.; Wasserman, Z. R. *Macromolecules* **1976**, *9*, 879–888.
(129) Hong, K. M.; Noolandi, J. *Macromolecules* **1981**, *14*, 727–736.
(130) Matsen, M. W.; Schick, M. *Phys. Rev. Lett.* **1994**, *72*, 2660–2663.
(131) Grest, G. S.; Kremer, K. *Phys. Rev. A* **1986**, *33*, 3628–3631.
(132) Morita, H.; Kawakatsu, T.; Doi, M.; Nishi, T.; Jinnai, H. *Macromolecules* **2008**, *41*, 4845–4849.
(133) Kawasaki, K.; Kawakatsu, T. *Macromolecules* **1990**, *23*, 4006–4019.
(134) Wissler, M. *J. Power Sources* **2006**, *156*, 142–150.
(135) Lin, W. F.; Iwasita, T.; Vielstich, W. *J. Phys. Chem. B* **1999**, *103*, 3250–3257.
(136) Antolini, E.; Giorgi, L.; Cardellini, F.; Passalacqua, E. *J. Solid State Electrochem.* **2001**, *5*, 131–140.
(137) Ferreira, P. J.; la O', G. J.; Shao-Horn, Y.; Morgan, D.; Makharia, R.; Kocha, S.; Gasteiger, H. *J. Electrochem. Soc.* **2005**, *152*, A2256–A2271.
(138) Gruber, T. C.; Zerda, T. W.; Gerspacher, M. *Carbon* **1993**, *31*, 1209–1210.
(139) Ito, T.; Matsuwaki, U.; Otsuka, Y.; Katagiri, G.; Kato, M.; Matsubara, K.; Aoyama, Y.; Jinnai, H. Direct three-dimensional visualization and morphological analysis of Pt particles supported on carbon by transmission electron microtomography. In *Handbook of Fuel Cells*; Vielstich, W., Gasteiger, H. A., Yokokawa, H., Eds.; John Wiley & Sons: Hoboken, NJ, 2009; Vol. *5*.
(140) van Bavel, S. S.; Sourty, E.; de With, G.; Loos, J. *Nano Lett.* **2009**, *9*, 507–513.
(141) Andersson, B. V.; Herland, A.; Masich, S.; Inganäs, O. *Nano Lett.* **2009**, *9*, 853–855.
(142) Hamley, I. *Prog. Polym. Sci.* **2009**, *34*, 1161–1210.